A TWO-PHASE MATERIAL APPROACH TO MODEL STEEL FIBRE REINFORCED SELF-COMPACTING CONCRETE IN PANELS

Amin Abrishambaf*[1], Vítor M.C.F. Cunha[1], Joaquim A. O. Barros[1]

[1] ISISE, Dep. Civil Eng., School Eng., University of Minho, Campus de Azurém 4800-058 Guimarães, Portugal

ABSTRACT

This work presents an experimental and numerical approach to ascertain the mechanical behaviour of steel fibre reinforced self-compacting concrete in laminar structures. Four-point flexural tests were performed on prismatic specimens extracted from a SFRSCC panel; the specimens' behaviour was then modelled under the FEM framework. SFRSCC is assumed as a two-phase material, i.e. plain concrete and discrete steel fibres. The nonlinear material behaviour of the plain matrix was simulated using 3D smeared crack model, while the fibre reinforcement mechanisms were modelled using micro-mechanical behaviour laws determined from experimental fibre pull-out tests. The good performance of the developed numerical strategy was demonstrated.

Keywords: Steel fibre reinforced self-compacting concrete; Flexural behaviour; Fibre orientation/distribution; Micromechanics; Finite element analysis.

* Author to whom the correspondence should be sent (amabrishambaf@gmail.com)
Tel: +351 253 510 210   Fax: +351 253 510 217

1. INTRODUCTION

In the past decades, the development of steel fibre reinforced self-compacting concrete (SFRSCC) technology for structural applications has been pushed forward by increasingly higher concrete construction industry requirements. The adoption of this material can partially, or even fully, exclude the use of conventional steel reinforcement, since steel fibres are able to provide significantly higher post-cracking tensile strength than an equivalent strength class unreinforced self-compacting concrete (SCC). Several researchers have shown that the incorporation of discrete fibres can improve both toughness and durability of concrete due to the crack width restraint [1-3]. However, the tensile performance of SFRSCC, and in particular the post-cracking strength, depends, among other factors, on how fibres are distributed and oriented in the matrix, since this also contributes to the grade of fibre reinforcement efficiency. In laminar structures, a proper knowledge and better understanding of the fibre distribution/orientation parameters can enable a better estimation of the material post-cracking strength and, consequently, to reduce the material properties scatter [4]. In order to accurately predict the tensile behaviour of SFRSCC, it is crucial to understand how fibres are distributed, as well as oriented within the composite bulk. In the case of SFRSCC, fibre distribution/orientation is influenced, mainly, by the properties in the fresh state of concrete (flowability) and wall effects [4-6]. This leads to the variation of the post-cracking parameters through the specimen. Therefore, assuming SFRSCC as an isotropic material could lead to an unrealistic estimation of the mechanical performance of a certain structural element.

In general, the stress – crack opening displacement relationship, $\sigma - w$, can be used to estimate the post-cracking response of low content fibre reinforced concrete [7]. Several analytical micro-mechanical models are available in literature to predict the tensile performance of steel fibre reinforced concrete, SFRC, assuming a random fibre distribution [8-11]. These models are principally based on averaging the contribution of the individual fibres transferring stresses across a crack plane. However, in the case of SFRSCC structures, an anisometric fibre structure was expected, mainly, due to the high flowability of the self-compacting concrete [4]. In addition, the post-cracking behaviour of the composite is also strongly influenced by the micro-mechanical properties of a single fibre. In fact, the knowledge of the fibre bond stress – slip behaviour, conjugated with an accurate fibre distribution, can render a good estimation of the composite mechanical properties [12]. SFRSCC can be assumed and modelled as a two–phase material, namely, the plain concrete phase (aggregate and paste) and the fibre phase. The first one is

considered as a homogeneous phase, while the latter one comprises the information regarding to the fibre density and orientation considering the influence of concrete flowability and also wall effects.

In the present work, an experimental program and a numerical approach for modelling SFRSCC in laminar structural elements are presented. SFRSCC was assumed as a two-phase material comprising one homogeneous phase representative of aggregates and paste, and a second phase that includes all the discrete fibres. The random fibre distribution was obtained with an algorithm based on the Monte Carlo method [13], which provided a realistic distribution of fibres through the bulk. The unreinforced concrete phase was modelled using solid finite elements, while fibres were modelled using 3D embedded elements. The geometry, position and orientation of the fibres were inserted into the solid finite element mesh to generate a heterogeneous mesh. A 3D multidirectional fixed smeared crack model was used to simulate the fracture process of the cementitious matrix. Furthermore, in order to simulate the fibre/matrix interface properties, a nonlinear behaviour was assigned to each fibre. These interface behaviour laws were obtained from fibre pull-out tests with distinct fibre's inclination angles.

2. EXPERIMENTAL PROGRAM

A summary of the experimental program carried out by the authors is hereby presented. Further details can be found elsewhere [14, 15].

2.1. Concrete mixture

A SFRSCC was developed and designed with a maximum aggregate size of 12 mm. Table 1 includes the mixture composition. Superplasticizer Sika® 3005 (SP) has been used to guarantee the required workability. Hooked-end steel fibres with length, l_f, of 33 mm, diameter, d_f, of 0.55 mm, aspect ratio, l_f/d_f, of 60, and a yield stress of 1100 MPa were used. The fresh concrete behaviour was determined by the Abrams cone slump test in the inverted position according to the EFNARC recommendations [16]. A total spread of 590 mm was measured.

1 Six cylinders with a diameter of 150 mm and a height of 300 mm were cast to evaluate the concrete compressive

2 strength. At the age of 28 days, the average compressive strength and Young's modulus were 72.3 MPa and 42.1

3 GPa with a coefficient of variation (CoV) of 8.23% and 0.26%, respectively.

4 Table 1: Mix composition of self-compacting concrete per m^3.

Cement [kg]	Water [kg]	W/C [–]	SP [kg]	Limestone filler [kg]	Fine sand [kg]	Coarse sand [kg]	Coarse aggregate [kg]
413	124	0.30	7.83	353	237	710	590

5 **2.2. Fibre pull-out test**

6 2.2.1. Specimens

7 The pull-out tests were executed on single-sided cylindrical specimens. A single steel fibre was embedded into a

8 cylindrical concrete specimen with 80 mm in height and diameter. For this purpose, a mould allowing the production

9 of 81 specimens at the same time ensuring a certain embedment length and orientation was used. Fig.1 shows the

10 specimen's manufacturing procedure. In this study 0, 30 and 60 degree fibre inclination angles were considered.

11 Cunha *et al.* [12] determined that the influence of the fibre embedment length was not so significant as the

12 orientation angle effect. However, if the fibre embedment length is lower than the length of the hooked end, the fibre

13 reinforcement contribution will be rather small, since the hook cannot be effectively mobilized. Therefore,

14 considering that the theoretical value of a fibre's embedded length bridging an active crack is $l_f/4 = 8.25$ mm [17],

15 this value was selected as the fibre's embedment length in the production of all the specimens. The pull-out tests

16 were executed on six specimens for each fibre's inclination angle.

(a)   (b)

Fibre

<div style="text-align:center">(c)</div>

<div style="text-align:center">(d)</div>

Fig. 1: Production of the specimens for fibre pull-out test: (a) Casting device, (b) Fibre installation in the mould, (c) Casting panel with SCC and (d) Extracted pull-out specimen.

2.2.2. Test set-up

The single-sided pull-out specimen was accommodated in a steel frame using a universal testing machine with a capacity of 50 kN. An HBM type S9 load cell with a capacity of 5 kN was also used to measure the load with enough accuracy. A steel ring was mounted on the top of the specimen. This was connected to the frame base plate using three screws disposed around the specimen forming an angle of 120°. Finally, the protruded end of the fibre was fastened into a standard LOYD® grip, which guaranteed a secure hold of the fibre. All the test set-up components are depicted in Fig. 2(a). During the test execution, the slip was measured with three linear variable diferential transducers, LVDTs, (linear stroke +/- 5 mm). The LVDTs were positioned on the back side of the grip, see Fig. 2(b). To ascertain the occurance of fibre slipage at the grip, a VMS-004D-400x USB Microscope with 2 Mega Pixels camera was used to capture the relative displacement between the fibre and the grip. The test was executed in closed-loop displacement control. A displacement rate of 1 μm/s was applied up to the slip of 2 mm, followed by 4 μm/s until the end of the test.
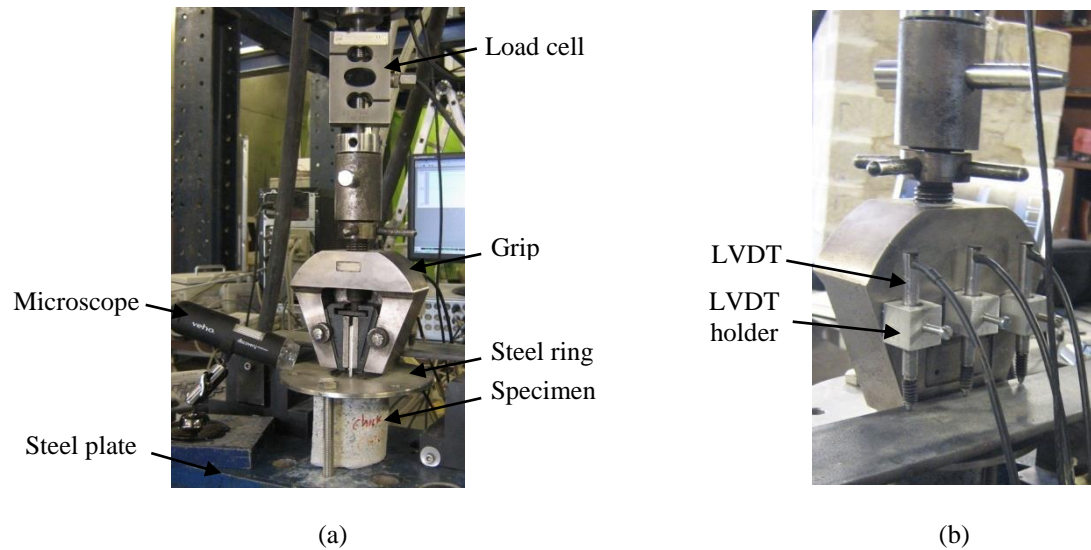
Fig. 2: Configuration of single fibre pull-out test: (a) Test components and (b) Connection of LVDTs.

2.2.3. Results and discussion

Fig. 3 shows the average pull-out load – slip relationship and correspondent envelope for the adopted fibre inclinations. The slip was determined by averaging the signals recorded in the three LVDTs installed on the backside of the grip. Two failure modes were observed: the aligned fibres were completely pulled-out, while the inclined fibres were ruptured. For the fibres with an inclination angle of 0°, the pre-peak branch consists of a linear and non-linear part. The linear part corresponds to the elastic behaviour of the bond, whereas the non-linear part could be ascribed to a mix of two mechanisms: degradation of the adhesion between the fibre and surrounding matrix, and the beginning of the end hook's mobilization process. After the peak load is attained, both curvatures of the hooked part are deformed progressively and thus, the pull-out load starts to decrease up to a slip of 3.5 mm. Finally, after the hook has been fully straightened, the pull-out process has occurred under frictional resistance. Fig. 3(b) depicts the pull-out load versus slip curve for fibres with an inclination angle of 30°. The pre-peak branch is similar to the fibres with 0° angle, but a slightly lower value of peak load was attained. This is due to the cracking and spalling of the matrix occurred at this fibre exit point in consequence of the deviational force component that fibre applies to this medium. Fig. 3(c) shows the pull-out load – slip relationship for the 60° specimens. In the first phase, the load has increased until the first evidence of matrix spalling. Afterwards, a matrix wedge was formed and gradually detached, which corresponds to the plateau branch of the load – slip relationship, while the fibre segment

6

1 embedded under this concrete portion was being straightened. After the completion of wedge spalling off, a new

2 equilibrium was attained and the pull-out fibre process has continued with a smaller stiffness until the fibre rupture.

3 More details regarding these results can be found in [14].

(a)

(b)

(c)
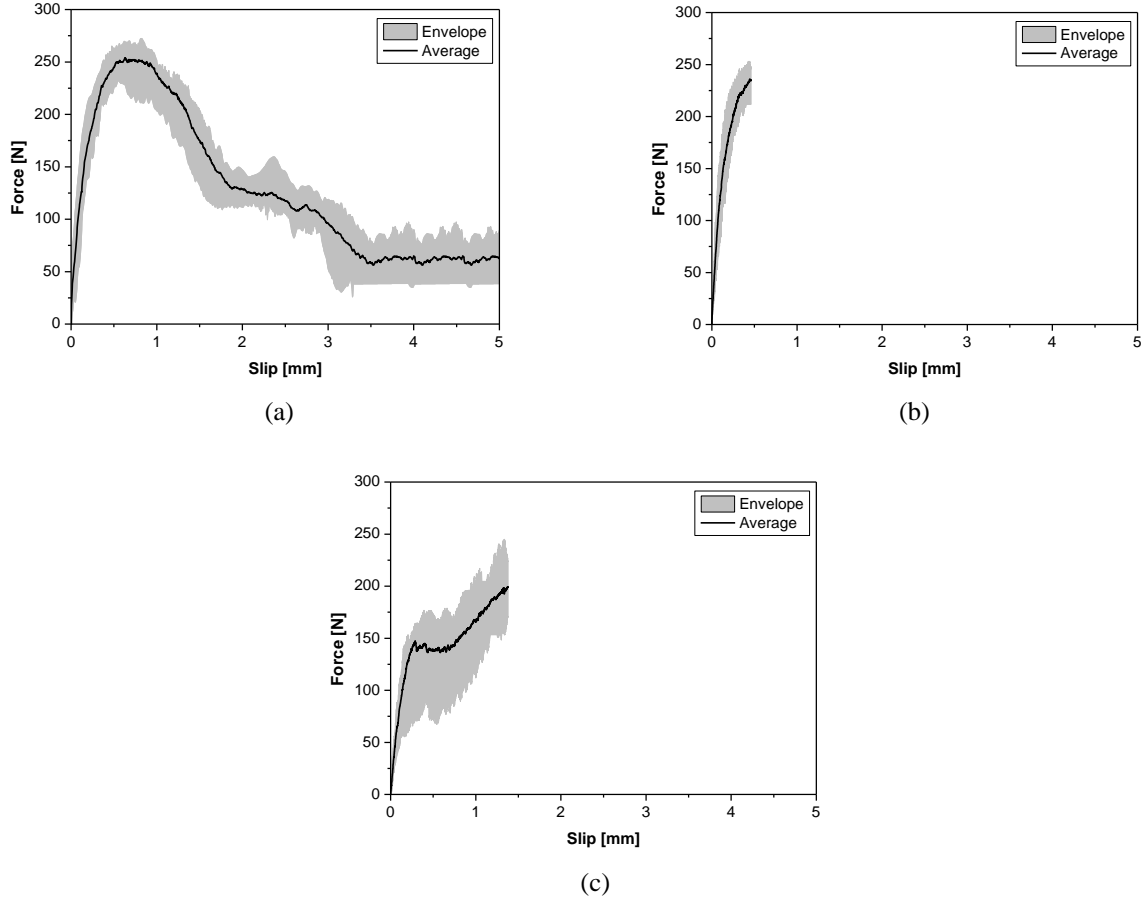
4 Fig. 3: Average monotonic pull-out load versus slip relationships for fibre inclination angles of: (a) 0°, (b) 30° and

5 (c) 60°.

6 **2.3. Monotonic four-point bending test**

7 2.3.1. Specimens

8 A panel of SFRSCC with the dimensions of 1500 mm × 1500 mm in plan and 60 mm of thickness was cast from its

9 centre. For the adopted casting conditions, previous research has revealed that a preferential radial distribution of

10 fibres through the panel will occur. Consequently, a higher number of effective fibres will be available for bridging

11 eventual cracks formed radially [18]. Therefore, the load carrying capacity of this type of panels, at serviceability

1 and ultimate limit state conditions, will be dependent on the crack patterns promoted by the loading and support

2 conditions of the panel. Considering the expected concrete flow direction, 60 prismatic specimens with dimensions

3 of 240 mm × 60 mm × 60 mm were extracted from the panel, see Fig. 4(a). In order to localize cracking during

4 testing, a notch with a depth of 10 mm and width of 2 mm was executed at half length of the specimen. To appraise

5 the influence of fibre orientation on the post-cracking behaviour, prismatic specimens were notched based on the

6 following methodology: by maintaining β as the angle between the expected concrete flow and notch direction, four

7 series of prismatic specimens with different preferential fibre orientations relative to the notch plane were derived

8 out, see Fig. 4(b). Four intervals for the angle β were considered, i.e. [0-15°), [15-45°), [45-75°) and [75-90°].

9 Hereinafter, each series was designated by a numeric string according to the following strategy: the first numeral

10 defines the β angle, in degrees, regarding the four intervals of the average relative orientation between the notched

11 plane and the SFRSCC flow directions (7.5°: [0-15°), 30°: [15-45°), 60°: [45-75°) and 82.5°: [75-90°]), while the

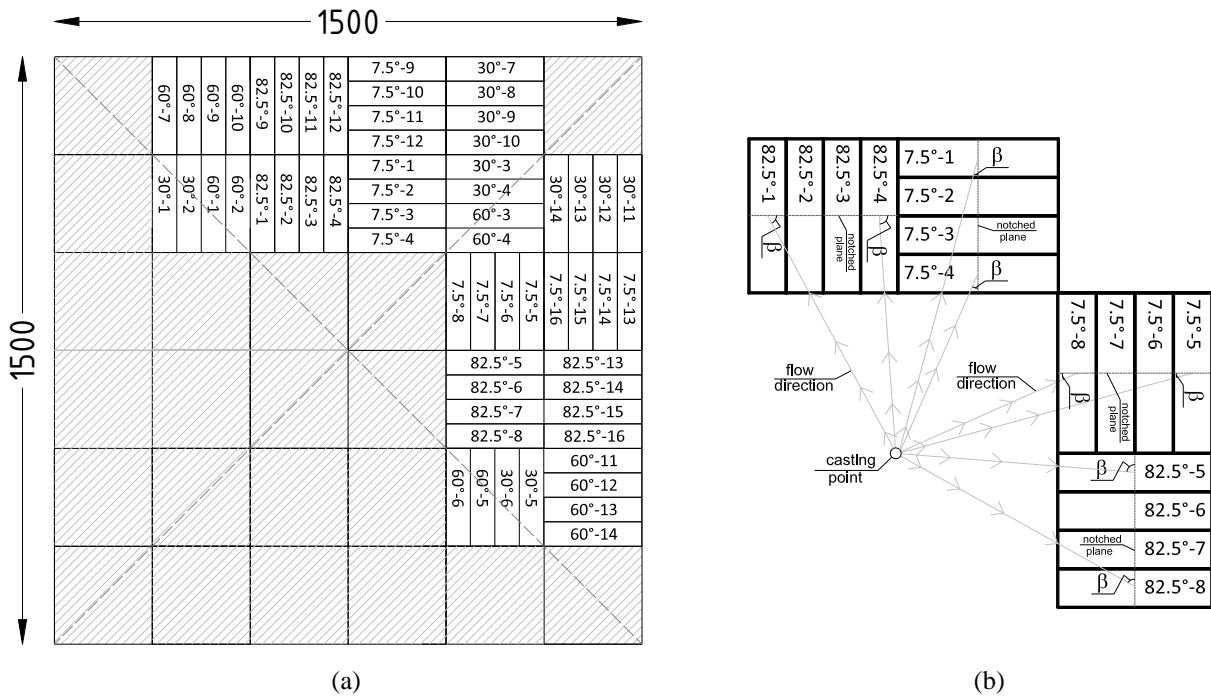12 second numeral refers to the specimen's number.

(a)   (b)

13   Fig. 4: (a) Specimen's extracting plane and (b) Definition of β angle.

14 2.3.2. Test set-up

15 The force – crack mouth opening displacement, F – CMOD, relationships were obtained from four-point bending

16 tests based on the Italian Standard UNI 11039 [19]. According to this standard, the lateral face of the specimen

8

1   coincides with the surface of the SFRSCC panel in contact with the mould, and the notch was executed on a face

2   parallel to the casting direction. Therefore, the bottom face of the specimen in the test set-up corresponds to a lateral

3   surface of the extracted beam from the panel, i.e. the beam was rotated by 90º along its longitudinal axis for testing.

4   The test was performed on a 50 kN loading capacity universal testing rig. A prescribed displacement rate of 0.002

5   mm/s was applied. During execution of the test, deflection and CMOD were measured by installing one LVDT at

6   the mid-span of the specimen, and three LVDTs at the notch on the bottom surface of the specimen, according to the

7   configuration schematically depicted in Figs. 5(a) and (b), respectively. Fig. 5(c) illustrates the LVDT connection

8   details.
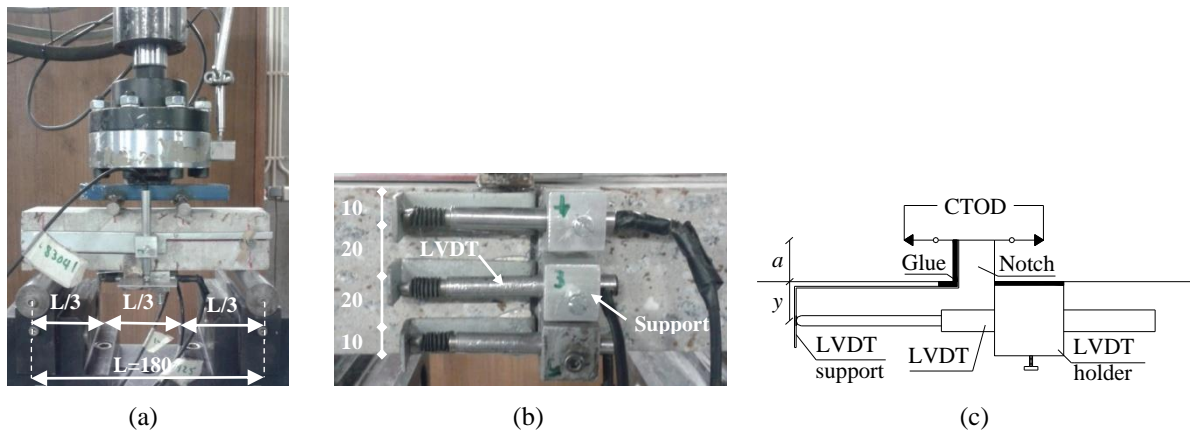
(a)   (b)   (c)

9   Fig. 5: Test set-up of the monotonic four-point bending test (dimensions are in mm): (a) Geometry of the specimen,

10   (b) LVDTs to record CMOD and (c) LVDT connection details for measuring CMOD.

11

12   2.3.3. Results and discussion

13   *2.3.3.1. Evaluation of fibre distribution and orientation*

14   The fibre distribution and orientation was assessed through an image analysis procedure, which was performed on a

15   parallel plane to the notch surface with an offset equal to half the length of the adopted fibre (Fig. 6), after

16   performing the monotonic four-point (4-P) bending tests. The following parameters were determined: i) the number

17   of fibres per unit area, N^f , which is the ratio between the total number of fibres counted in an image, N_T^f ,(counting

1   all the visible ellipses and circles at the cross section) and the total area of image, and ii) the fibre orientation factor,

2   η_θ, which was computed from Eq. (1):

3
$$\eta_\theta = \frac{1}{N_T^f} \cdot \sum_{i=1}^{N_T^f} \cos\theta_i \qquad (1)$$

4   where θ is the out-plane angle defined as the angle between the fibre's longitudinal axis and a versor orthogonal to

5   the cut plane. A summary regarding the steps involved on the execution of the image analysis technique can be

6   found in [4, 20].
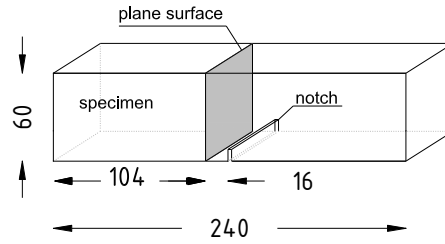
7

8   Fig. 6: Location of the plane surface in studied beams (dimensions are in mm).

9

10   Table 2 includes the fibre distribution parameters obtained by the image analysis technique. It was observed that N^f

11   and η_θ were higher in the specimens with the notched plane parallel to the expected concrete flow direction.

12   Moreover, these values tended to decrease when the notched plane rotated towards to the perpendicular position

13   regarding the flow direction. This can be justified due to the uniform velocity profile of concrete, which diffuses

14   radially and outwards from the centre of panel, as illustrated in Fig. 7. When casting a panel from its centre, fibres

15   tend to have a preferential orientation perpendicular to the concrete flow direction [4, 5, 21].

16

17   Table 2: Fibre distribution parameters obtained by image analysis technique.

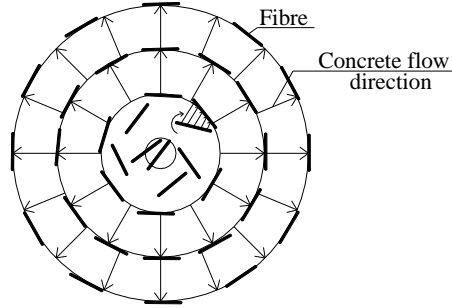|	Specimen	β = [0-15°)	β = [15-45°)	β = [45-75°)	β = [75-90°]
N^f [fibres/cm²]	Average	2.12	1.76	1.53	0.87
	CoV (%)	21.11	11.75	25.93	21.75
η_θ [-]	Average	0.875	0.807	0.73	0.672
	CoV (%)	1.01	4.37	6.36	12.94

Fig. 7: Explanation for fibre alignment in flowing concrete of a panel casting from the centre [4].

Fig. 8 shows the orientation probability density function based on the mean value and standard deviation of the fibre orientations (obtained from the image analysis results) for all series of notch plane orientations. The orientation of the fibres follows a Gaussian probability distribution [4]. From this figure, it is visible that when the range of angle β increases, the distribution function has progressively shifted to the right side, thus confirming that fibres have a tendency to be aligned more perpendicularly to the flow direction (see Figs. 4 and 7).
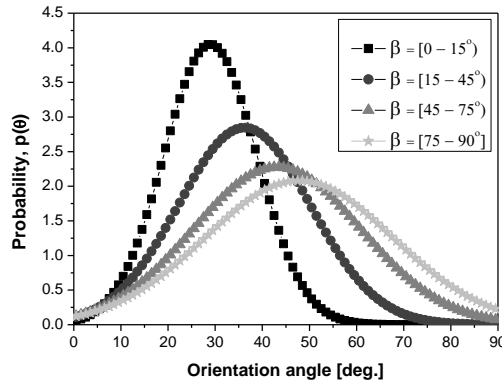
Fig. 8: Comparison between the predicted probability functions for all series of β.

2.3.3.2. Force – crack tip opening displacement relationships

Fig. 9 depicts the average and envelope experimental force – crack tip opening displacement relationships. The crack tip opening displacement, CTOD, was determined by averaging the values recorded by three LVDTs installed on the notch for each specimen (Fig. 5). The recorded value of crack mouth opening displacement ($CMOD_y$) was corrected to the CTOD as follows:
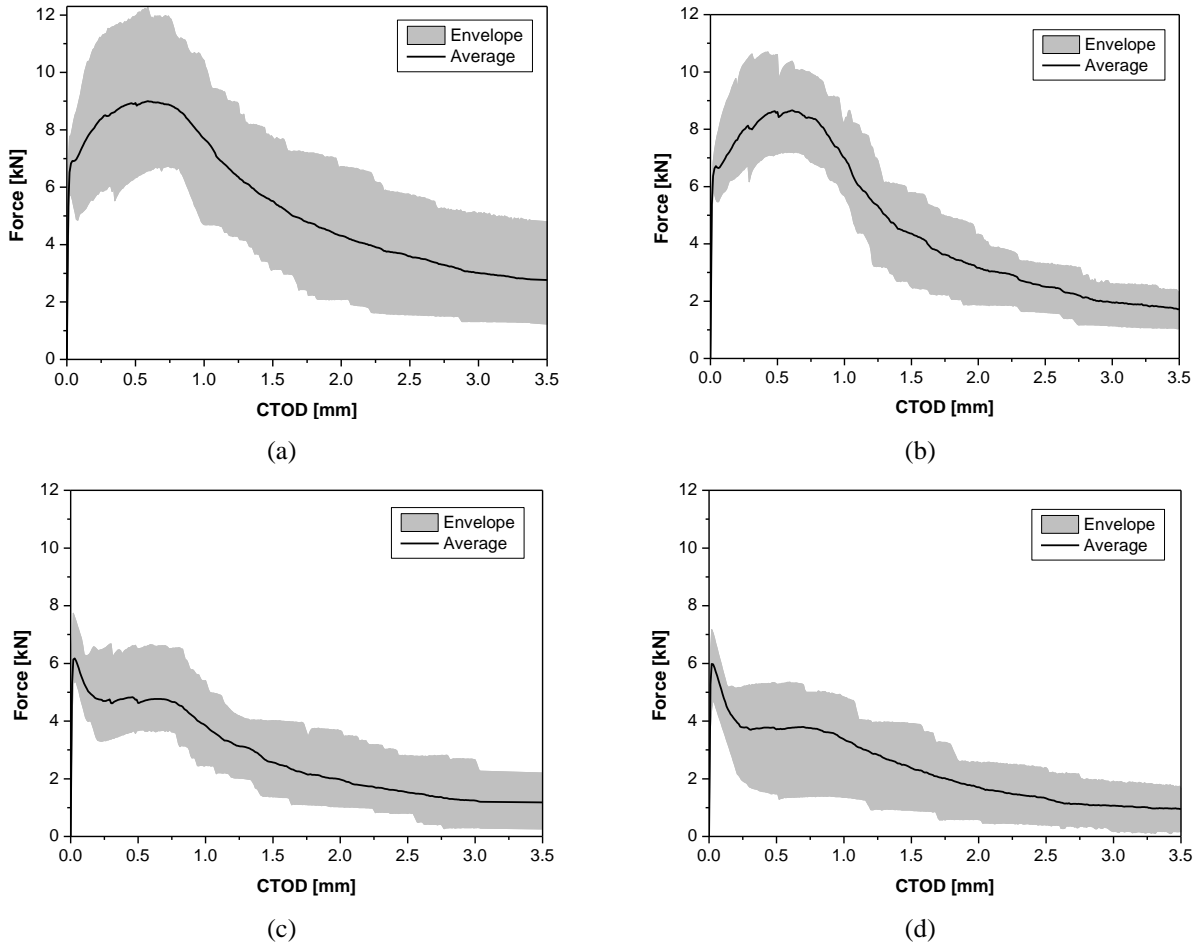
$$CTOD = CMOD_y \frac{h-a}{h+y} \qquad (2)$$

where, $CMOD_y$ is the recorded value in the LVDTs at a distance y below the notch mouth of the specimen, h is the

total depth of the specimen, and a is the depth of the notch.

Fig. 9: Monotonic four-point force – crack tip opening displacement response for β in the intervals: (a) [0-15°), (b)
[15-45°), (c) [45-75°) and (d) [75-90°].

In general, the specimens have shown a linear response up to the load corresponding to the crack initiation. A

similar load value at the limit of proportionality was observed for all the series. After the crack initiation, series with

β = [0-15°) and [15-45°) revealed a deflection-hardening response up to a CTOD nearby 0.65 mm, although β = [15-

45°) exhibited a slightly lower peak load. From the micro-mechanical point of view, after the fibre's adhesion to the

surrounding matrix has been exhausted, the fibre reinforcement mechanism was mainly governed by the

mobilization of the hooked end, which contributed for this deflection-hardening behaviour. After the peak load was

attained, a softening response was observed for both series. In the case of [0-15°) series, since the specimens had more fibres crossing the cracked plane with a lower orientation angle, the residual load decay was smoother, while for the β = [15-45°) specimens, a higher load decay was observable between 0.74 and 1.95 mm of CTOD.

Regarding the F – CTOD relationships for the [45-75°) and [75-90°] series, after the crack localization, the force dropped sharply up to a crack opening width between 0.18 – 0.20 mm, which then was followed by a plateau. Afterwards, a softening phase was observed in which the residual forces gradually decayed due to both fibre pull-out and rupture. Further details and discussion of the flexural responses can be found elsewhere [4, 15].

3. NUMERICAL SIMULATION

In this section, a three-dimensional numerical approach for modelling the SFRSCC four-point bending tests performed on specimens extracted from a panel (section 2.3) is presented and discussed. In this numerical approach, SFRSCC is assumed as a two-phase material, i.e. plain concrete and discrete steel fibres.

3.1. Concrete material model

In this numerical approach, the nonlinear behaviour of concrete was modelled with a 3D multidirectional fixed smeared crack model available in the FEM-based computer program FEMIX [22-24]. In the present case, it was assumed that at each integration point only one crack could be formed. To solve the system of nonlinear equations, an incremental iterative procedure was adopted. The relationship between the incremental strain and stress is defined as follows:

$$\Delta\underline{\sigma} = \underline{D}\Delta\underline{\varepsilon} \tag{3}$$

where $\Delta\underline{\sigma}$ is the stress vector increment, $\Delta\underline{\varepsilon}$ is the strain vector increment and $\underline{D}$ is the tangential constitutive matrix. In a smeared crack approach, the total incremental strain can be decomposed in an incremental crack strain vector, $\Delta\underline{\varepsilon}^{cr}$ plus an incremental strain vector of the concrete between cracks, $\Delta\underline{\varepsilon}^{co}$ [25, 26].

$$\Delta\underline{\varepsilon} = \Delta\underline{\varepsilon}^{cr} + \Delta\underline{\varepsilon}^{co} \tag{4}$$

1   To simulate the crack initiation and the fracture mode I propagation of plain concrete, the tri-linear diagram

2   represented in Fig. 10 was adopted. This diagram is defined by the parameters α_i and ξ_i, relating stress with strain at

3   the transitions between the linear segments that compose this diagram. The ultimate crack normal strain, $\varepsilon_{n,ult}^{cr}$, is

4   defined as a function of the parameters α_i and ξ_i; Mode I fracture energy, G_f^I; material tensile strength, $f_{ct} = \sigma_{n,1}^{cr}$;

5   and crack band width, l_b [22]. Table 3 includes the values of the model parameters used to simulate the plain

6   concrete behaviour.
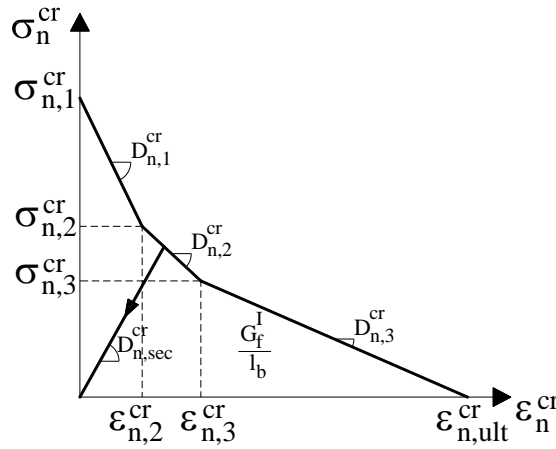
8   Fig. 10: Stress – strain relation based on the tri-linear law.

10   Table 3: Plain concrete properties used in the numerical simulations.

Density	25×10^{-6} N/mm^3
Poisson's ratio	0.2
Young's modulus	41.5×10^3 N/mm^2
Compressive strength	72 N/mm^2
Tri-linear tension-softening diagram	f_{ct} =4.66 N/mm^2; ξ_1=0.09; α_1=0.2; ξ_2=0.23; α_2=0.17
Fracture energy	0.118 N/mm
Crack band-width	l_b=2 mm

14

Fig. 11 depicts the three-dimensional mesh adopted for modelling the fracture process of the concrete matrix. In the present mesh, 5304 Lagrangian 8-noded solid elements with maximum and minimum volumes of 10 mm × 5 mm × 5 mm = 250 mm^3 and 2 mm × 5 mm × 5 mm = 50 mm^3, respectively, were used. Preliminary analyses were carried out in order to obtain a mesh refinement that does not compromise both the accuracy of the numerical simulations and the computational demands. The loading and boundary conditions of the model were applied according to the particularities of the test set-up, see Fig. 11. To localize the crack formation at the notch region, the nonlinear behaviour was assigned to the elements above the notch zone (at the mid-span of the specimen), while to the remaining solid elements was assigned a linear elastic behaviour. Furthermore, 1 × 2 × 2 and 2 × 2 × 2 Gauss-Legendre integration schemes were adopted for the elements above the notch, and the rest of elements, respectively (Fig. 11). The numerical analyses were performed under displacement control with 0.002 mm increment at mid-span vertically, using the arc-length method.
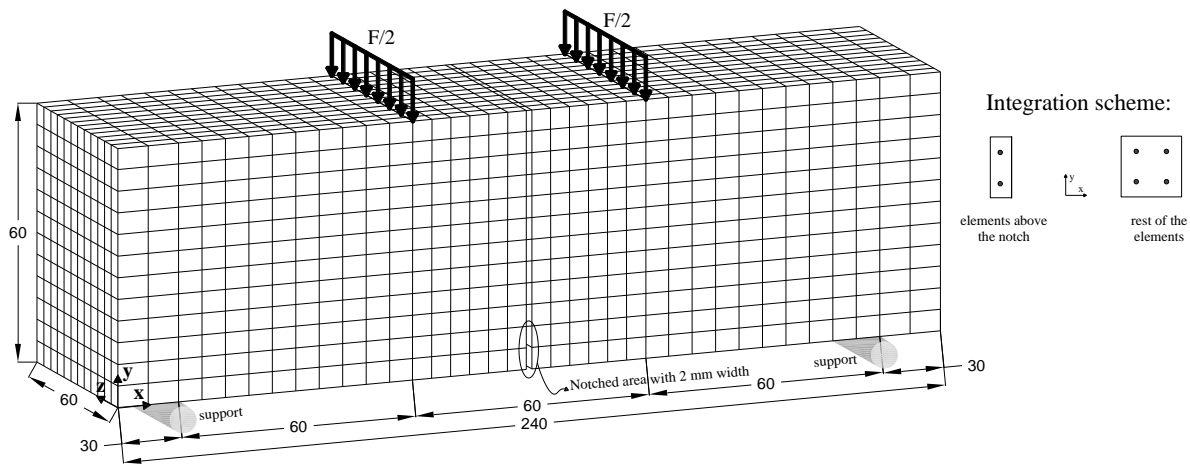

Fig. 11: Three – dimensional mesh of bulk concrete.

3.2. Fibre structure modelling

3.2.1. Fibre distribution

In this numerical approach, the fibre structure comprised the random distribution of the discrete fibres in the bulk concrete. This distribution was achieved with a Monte Carlo procedure. The fibre distribution procedure is summarized as follow [13].

1   (a)   The initial parameters were defined, namely: the content and geometrical data of fibres (fibre length, cross

2   sectional area and mass weight of a single fibre) and geometry of specimen as well as its dimensions.

3   (b)   Initializing the random number generation engine using the Mersenne-Twister (MT) procedure, which

4   generates uniform pseudo-random values.

5   (c)   The total number of fibres contained in the specimen was computed from the following equation:

6
$$N_f^{vol.} = V_{sp} \cdot \frac{C_f}{m_f} \tag{5}$$

7   where, V_{sp} is the volume of specimen, C_f is the fibre content [kg/m^3] and m_f [kg] is the mass weight of a

8   single fibre. Hereinafter, the next steps were repeated until $N_f^{vol.}$ was attained.

9   (d)   The fibre's gravity centre coordinates, as well as its orientation were randomly generated. It was observed

10   that the Gaussian distribution provided an accurate prediction of the fibre orientation profile in laminar

11   specimens [4]. Thus, in order to have a realistic numerical fibre distribution, the Gaussian probability

12   functions, see Fig. 8, were adopted to generate the orientations of each single fibre.

13   (i)   A set of three uniform random numbers (between 0 and 1), (ξ_x , ξ_y , ξ_z), were generated and the centre

14   of gravity coordinates were determined, (x_i , y_i , z_i), for the ith fibre:

15
$$\begin{aligned} x_i &= \xi_x b_{rct} \\ y_i &= \xi_y l_{rct} \\ z_i &= \xi_x h_{rct} \end{aligned} \tag{6}$$

16   where, b_{rct} , l_{rct} and h_{rct} are width, length and height of the prismatic specimen.

17   (ii)   According to the specified values of mean and standard deviation provided for the Gaussian

18   distribution, a random value between 0 and 1 is generated for the dependent variable of the cumulative

19   distribution function. The fibre orientation was set as the independent variable, $x = \cos\theta_i$, and was

20   obtained by the inverse distribution function method [13].

21   (iii)   The fibre orientation versor $\hat{u}_i = (u_i, v_i, m_i)$ (see Fig. 12) was computed by randomly generating the

22   first two components and determining the other component by solving Eq. (7) using the Newton-

23   Raphson method.

$$\cos(\theta_i) = \hat{u} \otimes \hat{\upsilon} \qquad (7)$$

where, $\cos(\theta_i)$ indicates the fibre orientation towards the cut plane based on the cumulative distribution function calculated in the prior step, and $\hat{\upsilon}$ is the considered plane's normal versor (Fig. 12).
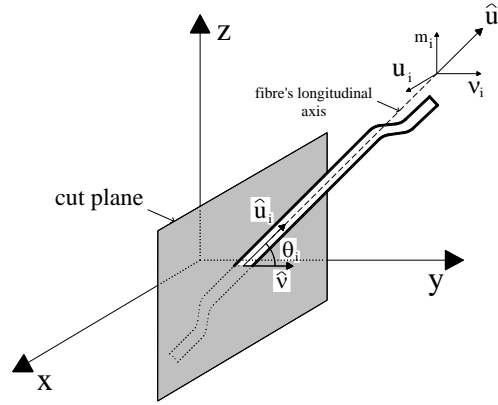
Fig. 12: Definition of fibre orientation versors.

(iv) The end-nodes' coordinates for the ith fibre ($j = 1,2$) were computed by:

$$\begin{aligned}
x_i^j &= x_i \pm l_f u_i / 2 \\
y_i^j &= y_i \pm l_f \upsilon_i / 2 \\
z_i^j &= z_i \pm l_f m_i / 2
\end{aligned} \qquad (8)$$

(v) Afterwards, it is necessary to check if the position of the ith fibre end-nodes coordinates complies with specimen's boundary conditions in Eq. (9). Since in this work, the prismatic specimens were extracted from a panel, it should be noted that the wall effects were mainly limited to the top and bottom surfaces of the specimens.

$$0 \le z_i^j \le h_{rct} \qquad (9)$$

(vi) For those fibres that did not satisfy the boundary conditions in Eq. (9), a new orientation was randomly generated to accomplish these conditions. Fig. 13(a) depicts a fibre structure complying with the

17

1   described boundary conditions. On the other hand, Fig. 13(b) shows a final fibre structure after

2   eliminating the fibres that intersected the lateral surfaces of the specimen. These fibres were not

3   considered, since in reality they were cut during the specimens' extraction from the cast slab.

4

(a)

(b)
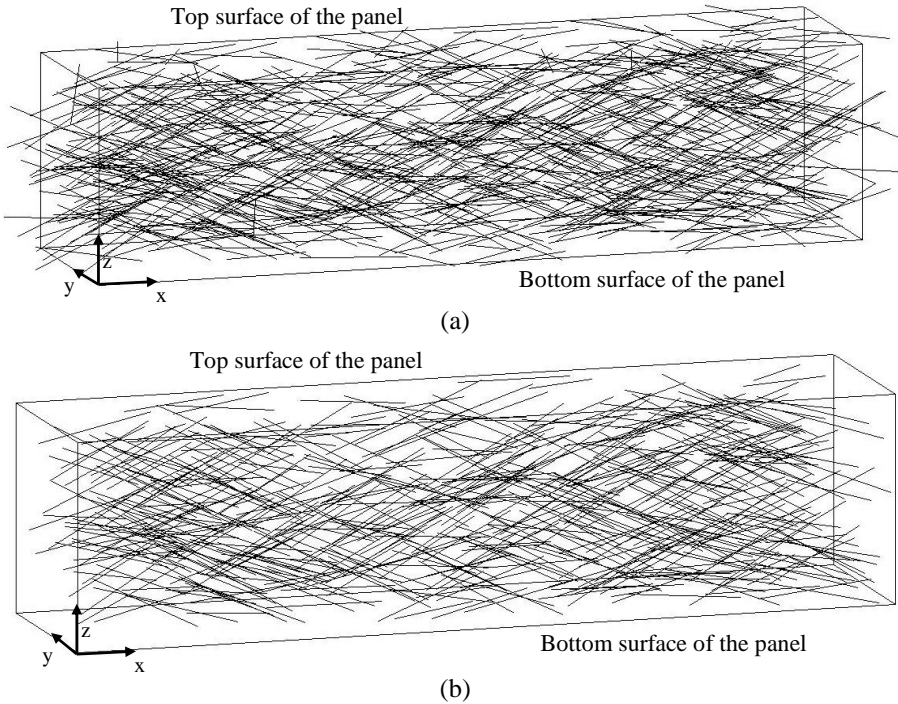
5   Fig. 13: Distribution of the steel fibres in the specimen: (a) Before and (b) After eliminating cut fibres.

6   (vii) Finally, the information regarding the fibre structure was saved into a data file.

7   Fig. 14 depicts the fibre structure meshes for the series β = [0-15°), [15-45°), [45-75°) and [75-90°]. It should be

8   noted that to maintain coherence with the adopted experimental procedure of the Italian Standard UNI 11039 [19],

9   the fibre structures were rotated by 90° along their longitudinal axis and the notch was modelled on a lateral surface

10   of the specimens. In this figure, it is possible to visualize the preferential fibre alignment due to the influence of the

11   concrete flow. In other words, it is visible that the fibres have rotated preferentially towards a perpendicular

12   direction of the concrete flow direction due to the radial nature and uniform velocity profile of the concrete flow, see

13   Fig. 7. To find out the accuracy level of the numerical fibre distribution, the latter distribution was compared with

14   the results obtained from the image analysis, at a same cross section's location. The total number of fibres, N_T^f, and

1   average fibre orientation factor, η_θ, obtained numerically were then compared with the experimental ones, see Table

2   4. The actual fibre distribution was accurately modelled with the aforementioned numerical approach.

(a)

(b)

(c)

(d)
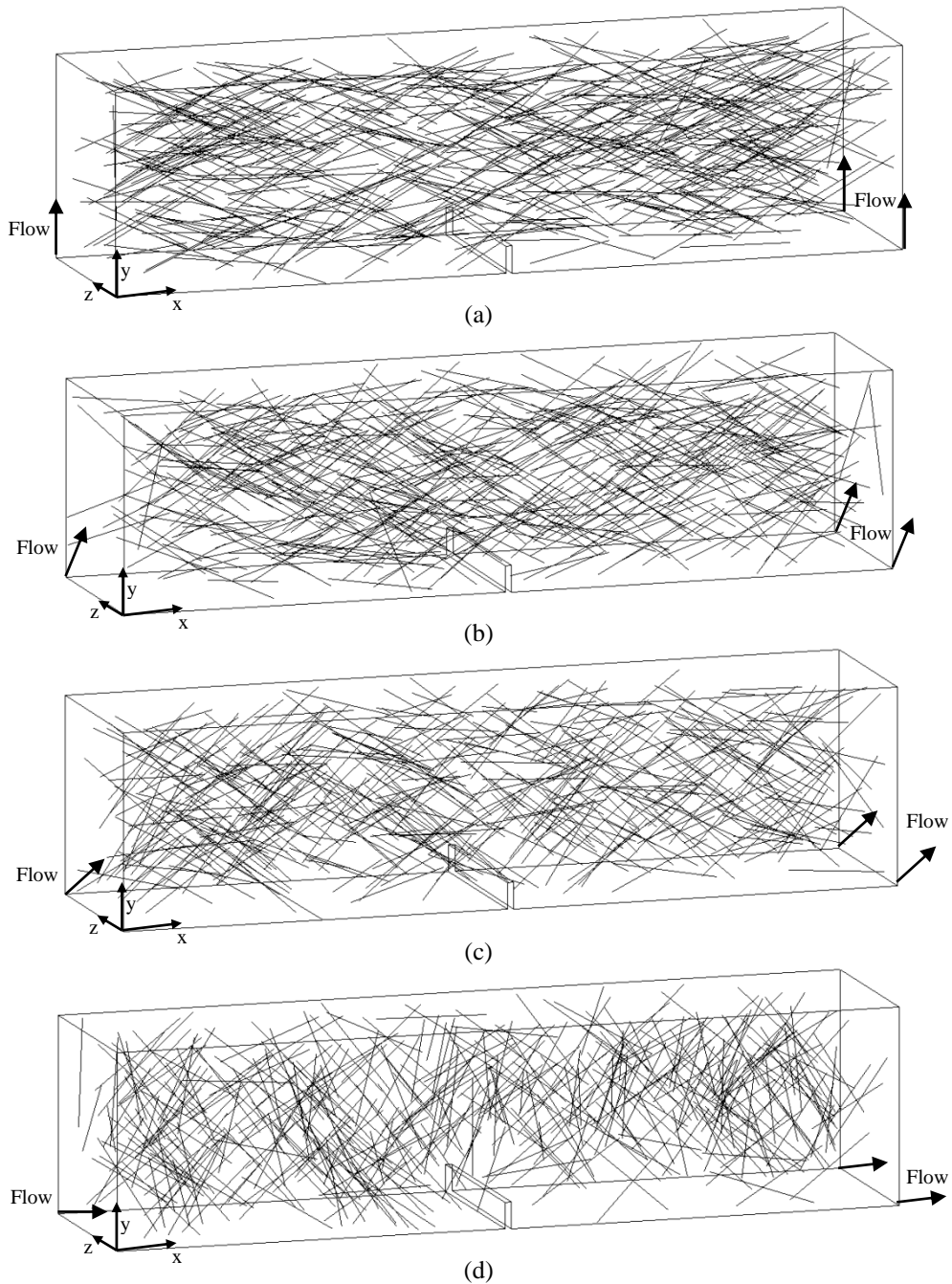
3   Fig. 14: Fibre distribution in a prismatic specimen extracted from a panel (the specimen's lateral face coincides with

4   the bottom surface of the panel, i.e. in contact with the mould): β = (a) [0-15°], (b) [15-45°], (c) [45-75°] and (d)

5   [75-90°].

1   Table 4: Comparison between image analysis results and numerical fibre distribution.

	Image analysis		Numerical distribution	
Series	N_T^f [fibre]	η_θ [-]	N_T^f [fibre]	η_θ [-]
[0-15°)	76	0.875	80	0.872
[15-45°)	70	0.807	76	0.807
[45-75°)	56	0.730	52	0.735
[75-90°]	31	0.672	38	0.677

2

3   After the generation of the meshes representative of the distinct fibre distributions observed through the panel, it was

4   inserted into the solid three-dimensional mesh, which modeled the fracture process of plain concrete, see Fig. 11.

5   The single fibre was modelled as an embedded element defined by two-end-nodes. Since an embedded element

6   corresponding to a fibre could intersect one or several solid elements, it was necessary to compute these intersection

7   points and divide the original finite element into distinct embedded elements to ensure compatibility between fibre

8   and solid meshes. For this purpose, an inverse mapping technique was employed to determine the coordinates of

9   these intersection points [27]. Finally, the stiffness matrix of a SFRSCC solid finite element, $\underline{K}^{rc}$, was determined

10   as follow [27]:

$$\underline{K}^{rc} = \underline{K}^{crco} + \sum_{i=1}^{n_f} \underline{K}_i^f \qquad (10)$$

12   where $\underline{K}^{crco}$, $\underline{K}_i^f$ and n_f are a solid finite element stiffness matrix (concrete), the stiffness matrix of the ith fibre

13   embedded in the concrete mother-element, and the total number of the embedded fibres in the mother-element,

14   respectively.

15   **3.2.2. Constitutive model for the embedded cables**

16   The embedded elements were modelled assuming a perfect bond between fibre and matrix. Therefore, the bond –

17   slip behaviour was modelled in an indirect fashion by converting the fibre load – slip, $F – s$, relationship into a stress

18   – strain, $\sigma_f – \varepsilon_f$, relationship. The $F – s$ relationship was determined by fitting the fibre pull-out test average curves

19   performed for three distinct inclination angles 0°, 30° and 60°. Each relationship was modelled with a three-linear

1   curve. Fig. 15 depicts this procedure, where ε_f, s and l_b are the fibre's strain, fibre's slip and the crack band width of

2   the solid finite element (width of the finite elements above the notch where the crack was forced to be formed, l_b=2

3   mm), whereas σ_f is the stress calculated from the pull-out force, F, divided by the fibre's cross section area, A_f. The

4   strain in an embedded element, ε_f, was obtained from the strain field of its mother-element and the corresponding

5   slip was determined multiplying ε_f by the crack band width, l_b. The tensile stress – strain relationship was assigned

6   to each fibre depending on its inclination angle, θ, between the fibre longitudinal axis and the normal versor of the

7   active crack surface, $\hat{n}$, (Fig. 16). Since assigning an individual $\sigma_f - \varepsilon_f$ law to each fibre with a particular

8   orientation angle and embedded length was not feasible, the three laws derived out from the fibre pull-out tests with

9   inclination angles, α, of 0°, 30° and 60° were used. The converted fibre pull-out responses for the series with α of 0°,

10   30° and 60° were ascribed to the embedded elements with θ ranging from [0-15°), [15-45°) and [45-75°),

11   respectively. It was assumed that the fibres with an inclination θ between [75-90°] were not mobilized. Table 5

12   includes the parameters of the tri-linear $\sigma_f - \varepsilon_f$ laws of the embedded elements with an angle θ.
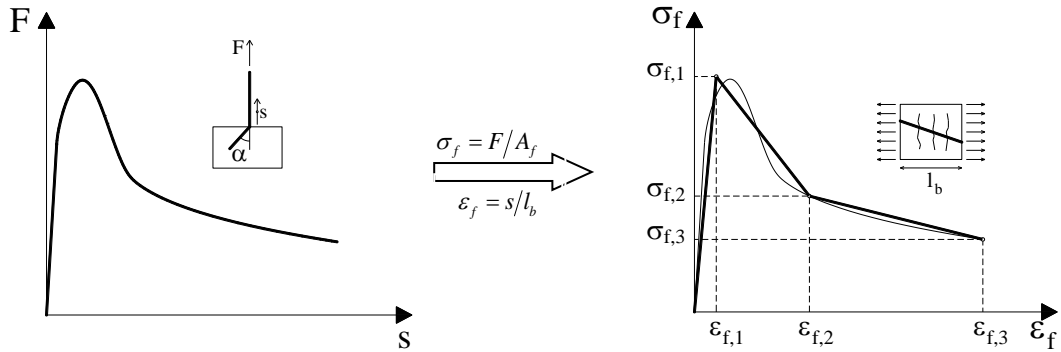
13   Fig. 15: Determination of the embedded cable's stress – strain diagram based on the experimental pull-out force –

14   slip relation.

15

16   Three-dimensional embedded elements with two integration points were used for simulating fibres. A Gauss-

17   Legendre integration scheme was adopted. All the embedded elements were ascribed with nonlinear behaviour.

18   Nevertheless, only the fibres intersecting an active crack were mobilized, while the other fibres remained in the

19   elastic regime.
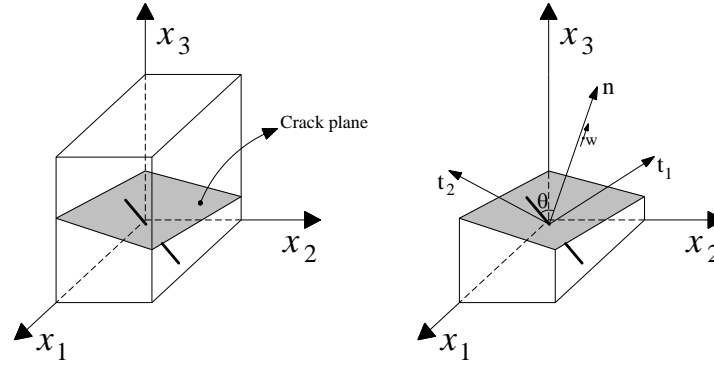
Fig. 16: Three-dimensional scheme of the embedded fibre intersecting an active crack (n is the vector normal to the crack plane).

Table 5: Tri-linear stress – strain relationships used for simulating the fibres' bond – slip behaviour.

α [°]	θ [°]	Failure mode	$\sigma_{f,1}$ [MPa]	$\sigma_{f,2}$ [MPa]	$\sigma_{f,3}$ [MPa]	$\varepsilon_{f,1}$ [-]	$\varepsilon_{f,2}$ [-]	$\varepsilon_{f,3}$ [-]
0°	[0-15)	Pullout	1060	558	240	0.33	1.23	2.4
30°	[15-45)	Rupture	200	770	1000	0.015	0.08	0.23
60°	[45-75)	Rupture	600	585	830	0.15	0.36	0.68

4. NUMERICAL RESULTS

Fig. 17 depicts a comparison between the average experimental F – CTOD relationship (Avg. EXP) and numerical simulation (NUM) for the studied ranges of the notch orientation. A good agreement between the numerical and experimental responses was obtained for all series. The force corresponding to the crack onset was predicted with high accuracy for all inclination angles of β. This was expected, since for low fibre content reinforced composites, the tensile strength is not significantly influenced by the fibre's distribution, orientation and mobilization. Regarding the series with β = [0-15°) and [15-45°), although the numerical simulations slightly underestimated the average peak load, they were still located within the experimental envelope.
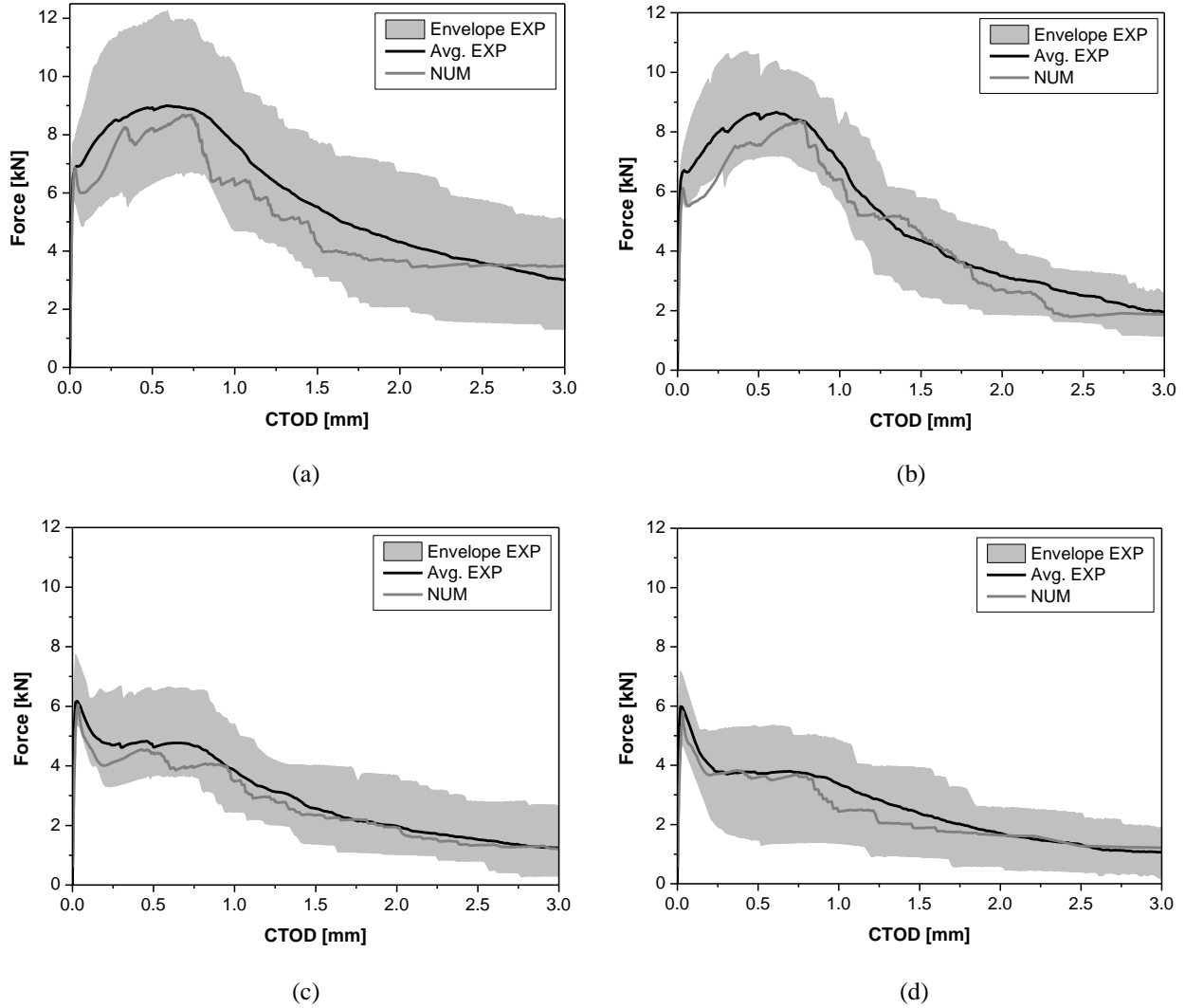
(a)

(b)

(c)

(d)

Fig. 17: Comparison between the experimental F – CTOD relationship and numerical simulation for β = (a) [0-15°], (b) [15-45°], (c) [45-75°] and (d) [75-90°].

Figs. 18(a) and 19(a) show the location of the embedded cables (fibres) that intersected the crack plane for the β = [0-15°] and [15-45°] series, respectively. Note that the any fibre intersecting the notch was removed from the finite element mesh. Figs. 18(b) and 19(b) depict, for the β = [0-15°] and [15-45°] series, the concrete tensile stresses orthogonal to the crack plane for a CTOD = 0.5 mm, which coincides with the crack opening width value used to compute the residual flexural strength f_{R1} [28]. It should also be mentioned that due to the high heterogeneity of the mesh (fibre orientation and distribution), the crack lost orthogonality during the numerical analysis. Consequently, the normal tensile stresses increased unrealistically due to numerical shear stress locking, mainly for higher crack

opening tip widths. However, in the present case, this did not influence significantly the flexural response since it

happens at the crack tip, i.e., near the cross section's neutral axis. The numerical stress locking was more

pronounced for the $\beta = [0\text{-}15°)$ and $[15\text{-}45°)$ series, since in these series a higher number of fibres has intersected the

crack plane, in contrast to the $\beta = [45\text{-}75°)$ and $[75\text{-}90°]$ series. Figs. 18(b) and 19(b) show that slightly higher

tensile stress values were transferred by the fibres in the $\beta = [0\text{-}15°)$ specimens, see also Table 6. This can be

ascribed to both a higher number of fibres in the fracture surface, as well as to a higher number of fibres aligned

more perpendicular to the crack plane. This can also be observed if one compares Figs. 18(c) and 19(c). These

figures show the normal tensile stresses due to the contribution of fibres and their surrounding matrix at the fracture

surface (the unrealistic high tensile stress values at the crack tip were ignored). The differences observed in the

grade of the residual flexural strengths between two series are more considerable after the peak load. Figs. 18(d) and

19(d) depict the normal tensile stresses at the crack plane for a CTOD = 2.5 mm corresponding to the one used to

compute the residual flexural strength f_{R3} [28]. It can be pointed out that the difference between the f_{R3} values

obtained for the distinct series, see Table 6, can be ascribed to the distinct micro-mechanical behaviour due to

distinct fibre orientation profiles in the $[0\text{-}15°)$ and $[15\text{-}45°)$ series. For the $\beta = [0\text{-}15°)$ specimens, fibre rupture did

not occurred so often since fibres crossed the crack plane with a lower average orientation angle, i.e. 29°. This can

be observed by comparing Figs. 18(e) and 19(e) (see the transferred stresses nearer the bottom of the fracture
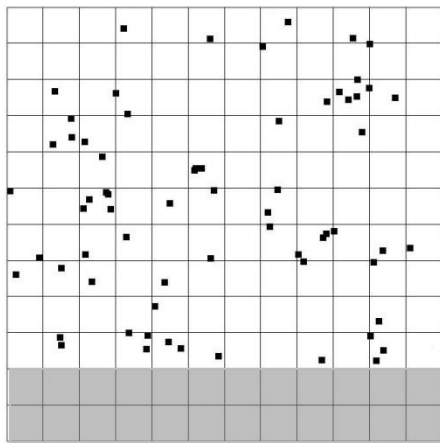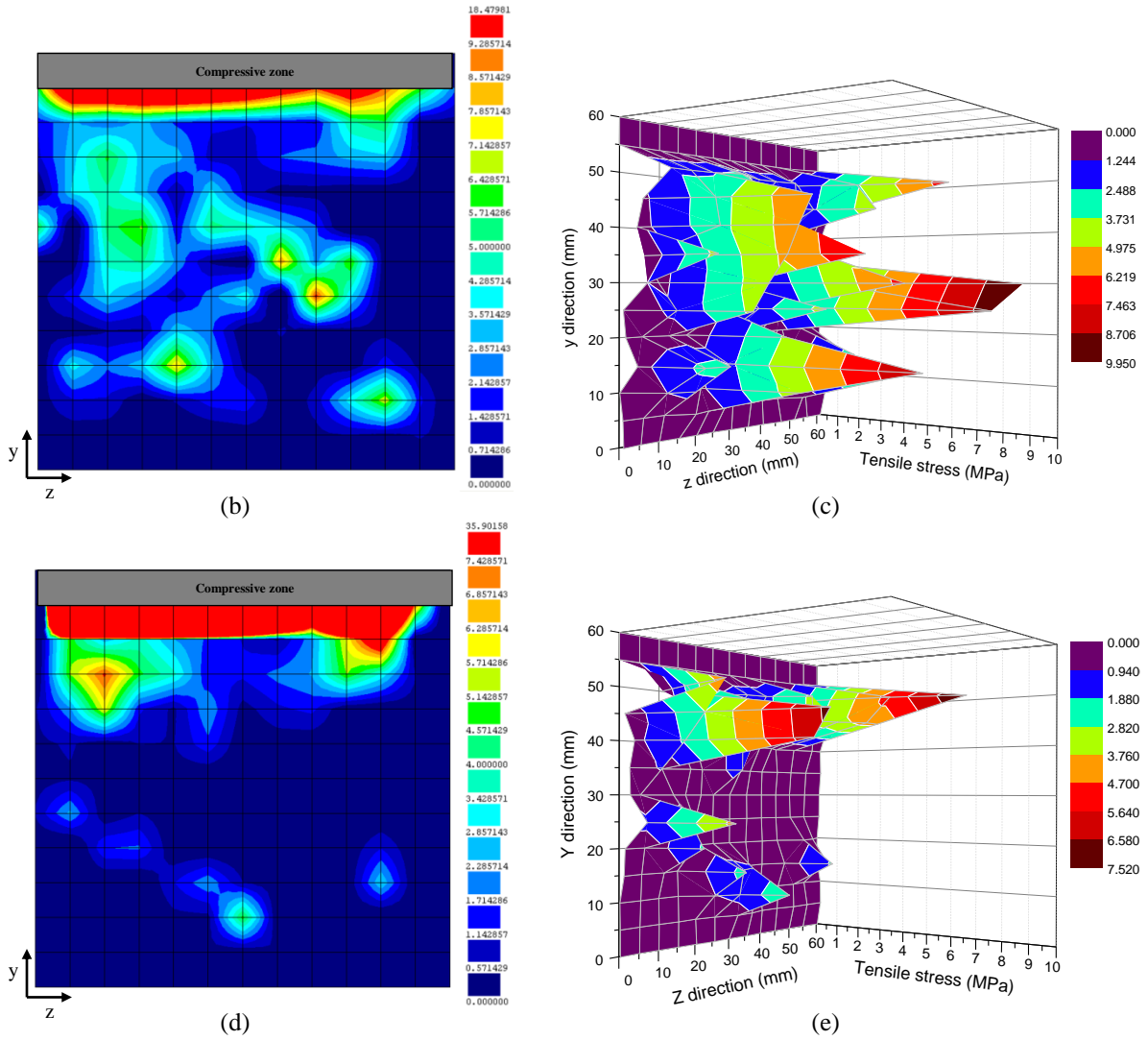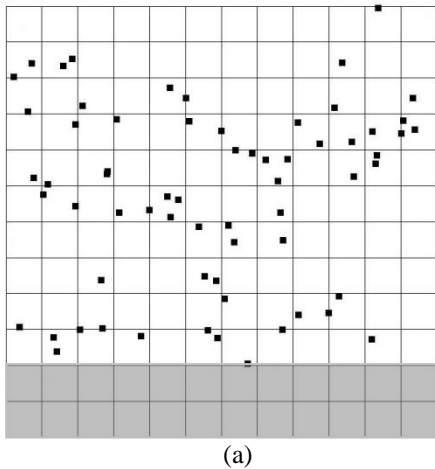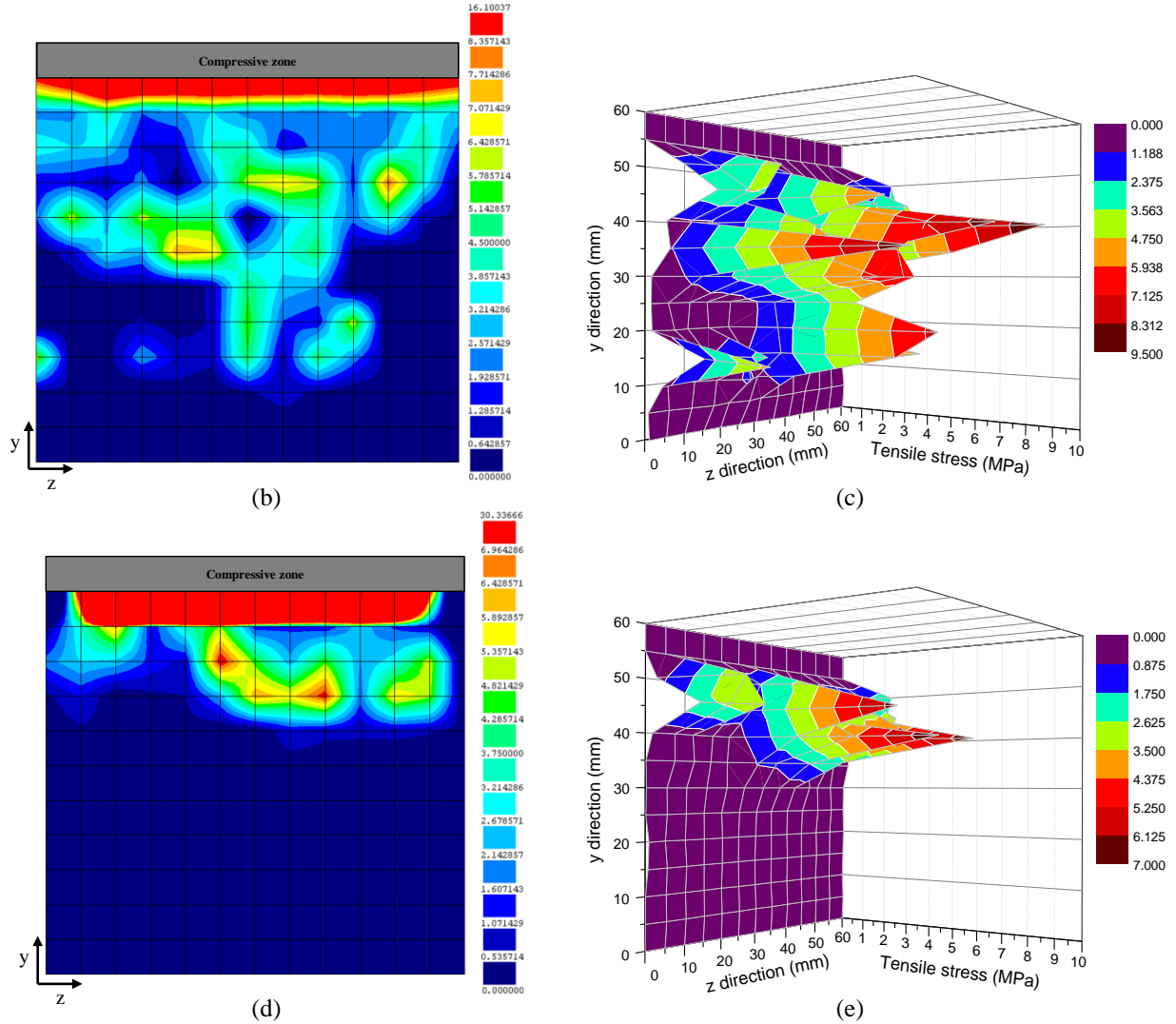
surface).

(a)

Fig. 18: Fracture surface for β = [0-15°) series: (a) Fibres at the crack plane (the gray area shows the notch location); (b) and (c) Normal concrete tensile stresses for a CTOD = 0.5 mm; (d) and (e) Normal concrete tensile stresses for a CTOD = 2.5 mm.
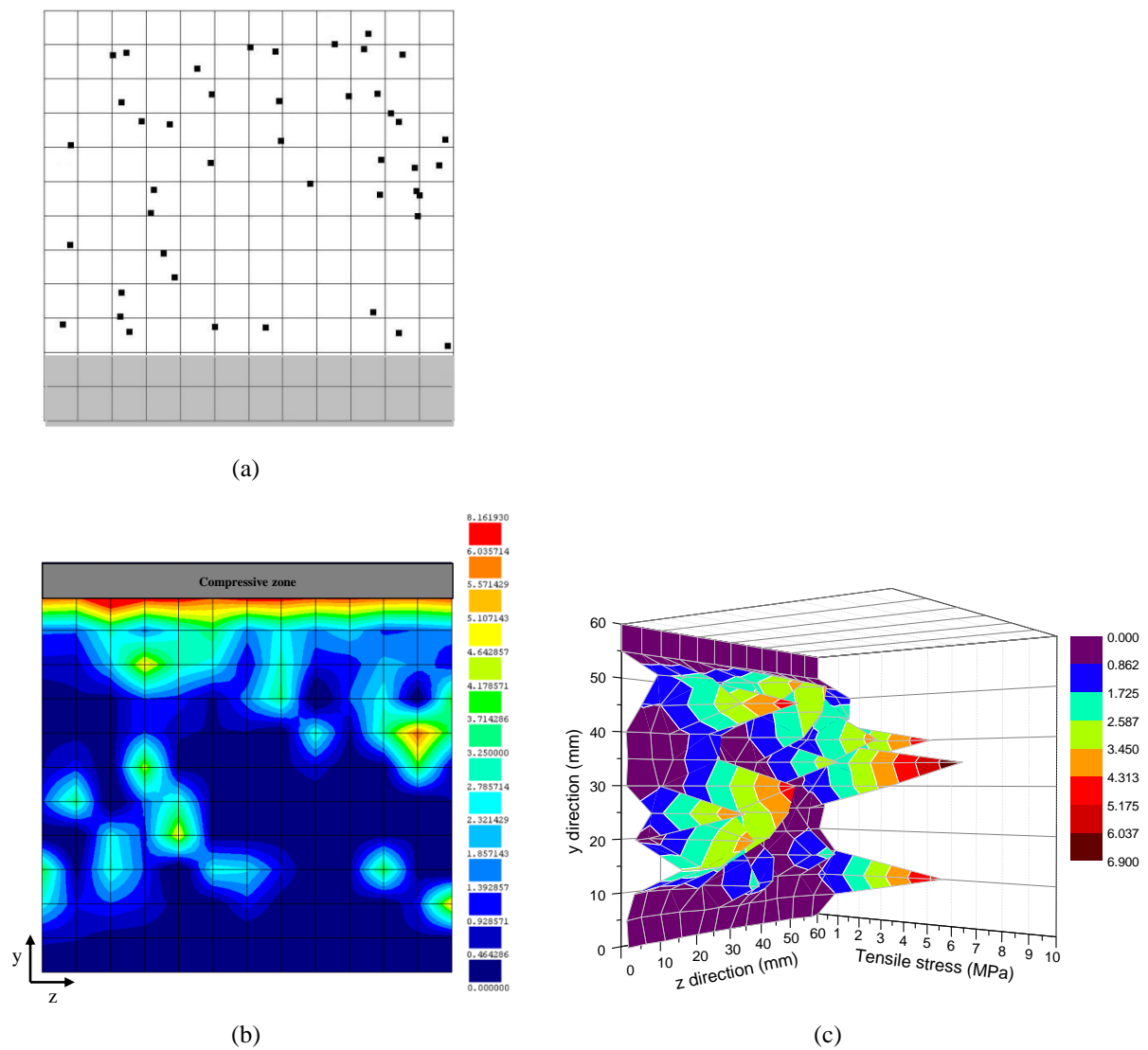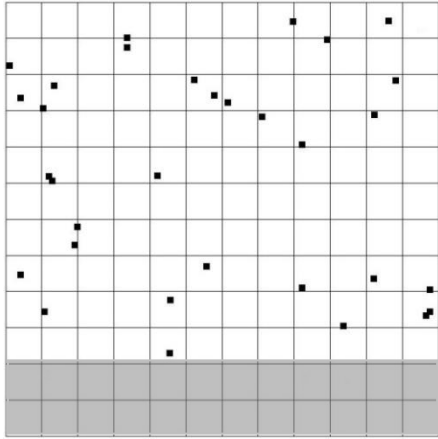
(b)

(c)

(d)

(e)

Fig. 19: Fracture surface for β = [15-45°) series: (a) Fibres at the crack plane (the gray area shows the notch location); (b) and (c) Normal concrete tensile stresses for a CTOD = 0.5 mm; (d) and (e) Normal concrete tensile stresses for a CTOD = 2.5 mm.

Figs. 20(a) and 21(a) show the location of the embedded elements (fibres) that intersected the crack plane for the β = [45-75°) and [75-90°] series, respectively. Moreover, Figs. 20(b), (c) and 21(b), (c) depict the normal tensile stresses at CTOD = 2.5 mm. As expected, the [45-75°) series exhibited higher stress values than the [75-90°] series, mainly, due to the higher number of fibres at the crack plane.

Table 6 compares residual flexural strengths f_{R1} and f_{R3} between all series. It was observed that β = [0-15°) series showed the highest residual flexural strengths. In terms of stress transfer capacity at the crack plane, this can also be observed by comparing Figs. 18(c), 19(c), 20(c) and 21(c). It was shown that higher stress levels were transferred

26

1 when the notch direction was more parallel to the flow direction. Therefore, when the angle β increased due to the

2 preferential orientation of fibres, caused by the concrete flow profile, the fibre orientation factor decreased, see

3 Table 4. This was translated by the reorientation of fibres more parallel to the crack plane during the casting

4 procedure. Therefore, in β = [0-15°) series, the specimens contained more effective fibres that intersected the

5 cracked plane with a lower orientation angle than other series. Moreover, the micro-mechanical response of the

6 aligned fibres (α = 0°) exhibited the highest pull-out load as well as the highest toughness, whereas for the inclined

7 fibres (α = 30° and 60°) the maximum pull-out load tended to decrease with the increase of the orientation angle, see

8 Fig. 3.

(a)

(b)   (c)

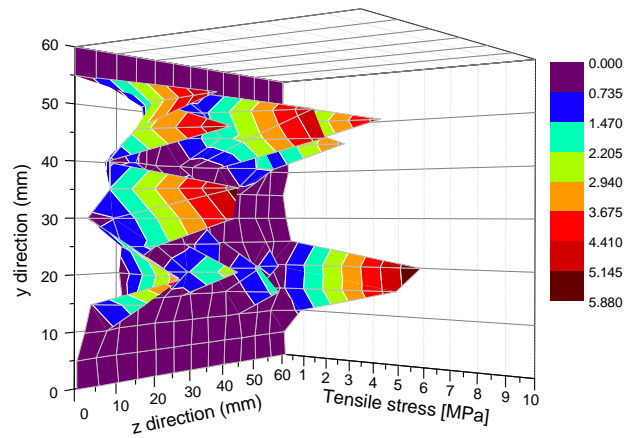9 Fig. 20: Fracture surface for β = [45-75°) series: (a) Fibres at the crack plane (the gray area shows the notch

10 location); (b) and (c) Normal concrete tensile stresses for a CTOD = 0.5 mm.
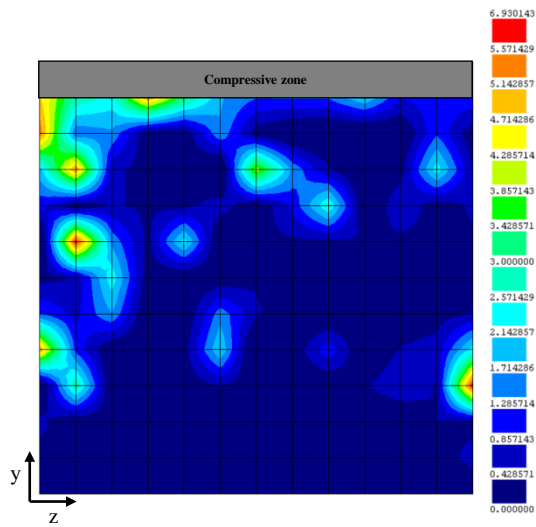
27

(a)

(b)

(c)

Fig. 21: Fracture surface for β = [75-90°] series: (a) Fibres at the crack plane (the gray area shows the notch location); (b) and (c) Normal concrete tensile stresses for a CTOD = 0.5 mm.

Table 6: Residual flexural strengths at CTOD = 0.5 mm (f_{R1}) and CTOD = 2.5 mm (f_{R3}) for different series.

f_{Ri} [MPa]	Series			
	[0-15°)	[15-45°)	[45-75°)	[75-90°]
f_{R1}	9.84	9.08	5.28	4.3
f_{R3}	4.21	2.20	1.60	1.53

5. CONCLUSIONS

In this research, an experimental program was presented and a numerical approach was proposed in order to model the behaviour of steel fibre reinforced self-compacting concrete, SFRSCC, laminar elements. The SFRSCC was modelled as a two-phase material, i.e. the fracture process of the concrete bulk was simulated with a 3D multi-directional smeared crack model, whereas the fibre phase was comprised by discrete randomly distributed embedded elements. The fibre structure randomly generated considered both the concrete flow and wall effects. The micro-mechanical behaviour of a single fibre was also considered. In order to simulate the fibre reinforcement mechanism, the force – slip laws obtained from the experimental pull-out tests were assigned to each fibre depending on its orientation angle towards the active crack plane.

From the experimental results of four-point bending tests, it was concluded that, due to the anisotropic fibre distribution/orientation, the post-cracking behaviour of SFRSCC was highly dependent on the directions in which the mechanical behaviours were evaluated. The specimens with the fracture surface more parallel towards the concrete flow direction, i.e. $\beta = [0\text{-}15°)$, presented higher residual forces, and thus a larger energy absorption capacity than the series with a notch plane more perpendicular to concrete flow direction.

Considering the methodology presented in this study, the experimental results of distinct four-point bending tests were modelled. The finite element simulations of the four-point-bending tests predicted with a high level of accuracy the experimental force – crack tip opening displacement relationships. Therefore, with a realistic prediction of the actual fibre distribution/orientation and having the knowledge of the micro-mechanical behaviour of the fibres, the mechanical behaviour of the SFRSCC composite could be predicted.

In spite of the good performance of the numerical model, in some series, after the crack initiation, the numerical response slightly underestimated the experimental average response. This could be ascribed to the fibres' constitutive laws determined in an indirect fashion from the fibre's load – slip relationships as well as due to the differences between the numerical (predicted) and experimental (real) fibre structures. Nevertheless, it should be mentioned that all numerical responses were comprised within the experimental envelope part.

ACKNOWLEDGMENT

REFERENCES

[1] Barros JAO, Cunha VMCF, Ribeiro AF, Antunes JAB. Post-cracking behaviour of steel fibre reinforced concrete. Materials and Structures 2005;38:47-56.

[2] Michels J, Christen R, Waldmann D. Experimental and numerical investigation on postcracking behavior of steel fiber reinforced concrete. Engineering Fracture Mechanics 2013;98:326-349.

[3] Zerbino RI, Barragan BE. Long-term behaviour of cracked steel fibre-reinforced concrete beams under sustained loading. ACI Material Journal 2012;109:215-224.

[4] Abrishambaf A, Barros JAO, Cunha VMCF. Relation between fibre distribution and post-cracking behaviour in steel fibre reinforced self-compacting concrete panels. Cement and Concrete Research 2013; 51:57-66.

[5] Boulekbache B, Hamrat M, Chemrouk M, Amziane S. Flowability of fibre-reinforced concrete and its effect on the mechanical properties of the material. Construction and Building Materials 2010; 24:1664-1671.

[6] Ferrara L, Ozyurt N, di Prisco M. High mechanical performance of fibre reinforced cementitious composites: the role of casting-flow induced fibre orientation. Materials and Structures 2011;44:109-128.

[7] Abrishambaf A, Barros JAO, Cunha VMCF. Tensile stress - crack width law for steel fibre reinforced self-compacting concrete obtained from indirect (splitting) tensile tests. Cement and Concrete Composites 2015;57:153-165.

[8] Lee SC, Cho JY, Vecchio FJ, Diverse embedment model for steel fibre-reinforced concrete in tension: Model development. ACI Material Journal 2011;108:516-525.

[9] Marti P, Pfyl T, Sigrist V, Ulaga T. Harmonized test procedures for steel fiber-reinforced concrete. ACI Materials Journal 1999;96:676-686.

[10] Tanigawa Y, Hatanaka S. Stress-strain relations of steel fibre reinforced concrete under repeated compressive load. Cement and Concrete Research 1983;13:801-808.

[11] Voo JYL, Fooster SJ. Variable engagement model for the design of fibre reinforced concrete structures. Advanced Materials for Construction of Bridges, Buildings, and Other Structures III, P05; 2003.

[12] Cunha VMCF, Barros JAO, Sena-Cruz JM. An integral approch for modelling the tensile behaviour of steel fibre reinforced self-compacting concrete. Cement and Concrete Research 2011;41:64-76.

[13] Cunha VMCF. Steel fibre reinforced self-compacting concrete - from micromechanics to composite behaviour. PhD Thesis, University of Minho, Portugal; 2010.

[14] Abrishambaf A, Barros JAO, Cunha VMCF. Determination of time-dependent behaviour of bond in steel fibre reinforced self-compacting concrete. 14-JUL/E-18, University of Minho, Portugal ; 2014.

[15] Abrishambaf A, Barros JAO, Cunha VMCF. Characterizing the time-dependent behaviour of cracked steel fibre reinforced self-compacting concrete panels, 14-July/E-19, University of Minho, Portugal; 2014.

[16] EFNARC, The European guidelines for self-compacting concrete; 2005.

[17] Stroeven P, Hu J. Effectivness near boundaries of fibre reinforcement in concrete. Materials and Structures 2006;39:1001-1013.

[18] Barnett SJ, Lataste JF, Parry T, Millard SG, Soutsos MN. Assessment of fibre orientation in ultra-high performance fibre reinforced concrete and its effect on flexural strength. Materials and Structures 2010;43:1009-1023.

[19] UNI-11039, Steel fibre reinforced concrete, Part I: Definition, classification, specification and conformity, Part II: Test method for measuring first crack strength and ductility indexes. Italian Board for Standardization; 2003.

[20] Abrishambaf A, Barros JAO, Cunha VMCF. A state of art study on the fibre orientation and distribution in steel fibre reinforced concrete, 13-DEC/E-16, University of Minho, Portugal; 2013.

[21] Abrishambaf A, Barros JAO, Cunha VMCF. Assessment of fibre orientation and distribution in steel fibre reinforced self-compacting concrete panels. 8th RILEM International Symposium on Fibre Reinforced Concrete: Challenges and Opportunities (BEFIB), Guimaraes, Portugal; 2012.

31

[22] Sena-Cruz JM. Strengthening of concrete structures with near surface mounted CFRP laminate strips, PhD Thesis, Universidade do Minho, Portugal; 2005.

[23] Ventura-Gouveia A, Barros JAO, Azevedo A, Sena-cruz JM. Multi-fixed smeared 3D crack model to simulate the behaviour of fibre reinforced concrete structures. Challenges for Civil Construction, FEUP, Porto, Portugal; 2008.

[24] Ventura-Gouveia A. Constitutive models for the material nonlinear analysis of concrete structures including time-dependent effects, PhD Thesis, University of Minho, Portugal; 2011.

[25] Bazant Z, Gambarova P. Rough cracks in reinforced concrete. ASCE Journal of Structure Division 1980;106:819-842.

[26] de Barst R, Nauta P. Non-orthogonal cracks in smeared finite element model. Engineering and Computer, 1985;2:35-46.

[27] Cunha VMCF, Barros JAO, Sena-Cruz JM. A finite element model with discrete embedded elements for fibre reinforced composites. Computers and Structures 2012;95:22-33.

[28] CEB-FIP, Volume 1, Model Code 2010, Tomas Telford, Lausanne, Switzerland; 2012.

1   **FIGURES AND TABLES**

2 **List of Figures:**

3 Fig. 1: Production of the specimens for fibre pull-out test: (a) Casting device, (b) Fibre installation in the mould, (c)

4 Casting panel with SCC and (d) Extracted pull-out specimen.

5 Fig. 2: Configuration of single fibre pull-out test: (a) Test components and (b) Connection of LVDTs.

6 Fig. 3: Average monotonic pull-out load versus slip relationships for fibre inclination angles of: (a) 0°, (b) 30° and

7 (c) 60°.

8 Fig. 4: (a) Specimen's extracting plane and (b) Definition of β angle.

9 Fig. 5: Test set-up of the monotonic four-point bending test (dimensions are in mm): (a) Geometry of the specimen,

10 (b) LVDTs to record CMOD and (c) LVDT connection details for measuring CMOD.

11 Fig. 6: Location of the plane surface in studied beams (dimensions are in mm).

12 Fig. 7: Explanation for fibre alignment in flowing concrete of a panel casting from the centre [4].

13 Fig. 8: Comparison between the predicted probability functions for all series of β.

14 Fig. 9: Monotonic four-point force – crack tip opening displacement response for β in the intervals: (a) [0-15°], (b)

15 [15-45°], (c) [45-75°] and (d) [75-90°].

16 Fig. 10: Stress – strain relation based on the Tri-linear law.

17 Fig. 11: Three – dimensional mesh of bulk concrete.

18 Fig. 12: Definition of fibre orientation versor.

19 Fig. 13: Distribution of the steel fibres in the specimen: (a) Before and (b) After eliminating cut fibres.

20 Fig. 14: Fibre distribution in a prismatic specimen extracted from a panel (the specimen's lateral face coincides with

21 the bottom surface of the panel, i.e. in contact with the mould): β = (a) [0-15°], (b) [15-45°], (c) [45-75°] and (d)

22 [75-90°].

Fig. 15: Determination of the embedded cable's stress – strain diagram based on the experimental pull-out force – slip relation.

Fig. 16: Three-dimensional scheme of the embedded fibre intersecting an active crack (n is the vector normal to the crack plane).

Fig. 17: Comparison between the experimental F – CTOD relationship and numerical simulation for β = (a) [0-15°), (b) [15-45°), (c) [45-75°) and (d) [75-90°].

Fig. 18: Fracture surface for β = [0-15°) series: (a) Fibres at the crack plane (the gray area shows the notch location); (b) and (c) Normal concrete tensile stresses for a CTOD = 0.5 mm; (d) and (e) Normal concrete tensile stresses for a CTOD = 2.5 mm.

Fig. 19: Fracture surface for β = [15-45°) series: (a) Fibres at the crack plane (the gray area shows the notch location); (b) and (c) Normal concrete tensile stresses for a CTOD = 0.5 mm; (d) and (e) Normal concrete tensile stresses for a CTOD = 2.5 mm.

Fig. 20: Fracture surface for β = [45-75°) series: (a) Fibres at the crack plane (the gray area shows the notch location); (b) and (c) Normal concrete tensile stresses for a CTOD = 0.5 mm.

Fig. 21: Fracture surface for β = [75-90°] series: (a) Fibres at the crack plane (the gray area shows the notch location); (b) and (c) Normal concrete tensile stresses for a CTOD = 0.5 mm.

List of Tables: